Journal of Molecular Structure 1277 (2023) 134895

Contents lists available at ScienceDirect

Journal of Molecular Structure

journal homepage: www.elsevier.com/locate/molstr

DFT investigations and molecular docking as potent inhibitors of SARS-CoV-2 main protease of 4-phenylpyrimidine

Sibel Celik

Vocational School of Health Services, Ahi Evran University, Kırşehir 40200, Turkey

ARTICLE INFO

Article history:
Received 17 November 2022
Revised 24 December 2022
Accepted 30 December 2022
Available online 30 December 2022

Keywords:
4-Phenylpyrimidine
Vibrational spectra
Molecular docking
ELF
COVID-19

ABSTRACT

In this work, quantum chemical descriptors and a vibrational analysis of 4-Phenylpyrimidine (4-PPy) were also investigated. Through conformational analysis, the most stable conformer can be determined. The geometry of the molecular structure was optimized by using the density functional theory (DFT) at the B3LYP/6–311++G(d,p) level. The theoretically obtained FT-IR and FT-Raman spectral data agree with the experimental results. UV–Vis was done in the gas phase along with different solvents by the TD-DFT method and the PCM solvent model. Molecular electrostatic potential, natural bond orbital analysis, nonlinear optical properties, and global chemical reactivity parameters were described through the DFT method. Besides, the chemical implications of a molecule were explained using an electron localization function and a local orbital locator. We attempted to detect the antiviral activity of the 4-PPy compound by predicting molecular docking into coronavirus 2 (SARS-n-CoV-2) protein structures (6LU7, 6M03, and 6W63), because COVID-19 is known to have serious adverse effects in all areas of human life worldwide, and possible drugs need to be investigated for this. The results of the docking simulation demonstrate good affinities for binding to the receptors.

1. Introduction

Pyrimidine derivatives are an interesting class of heterocycles with remarkable biological and pharmacological activities [1]. Compounds containing a pyrimidine core have a range of diverse biological activities such as antibacterial [2], antifungal [3], anti-inflammatory [4], antihypertensive [5], antiviral [6], anti-HIV [7], antidiabetic [8], anti-allergic [9], herbicidal [10] and anticancer [11–13]. Most of the sugar, vitamins, and alkaloids are nitrogenous bases, which are found in many antibiotics like penicillin [14].

The pyrimidine ring is significantly distributed in nature due to its existence in deoxyribonucleic acid (DNA) and ribonucleic acid (RNA) as nitrogenous bases. As a result, because pyrimidine bases are found in both DNA and RNA, they can be used to treat both DNA and RNA viruses [15]. Compounds with N-heterocyclic scaffolds are highly effective against a diverse range of diseases, and they have already been studied for their potential pharmacological activities. In an in-silico study, Rane et al. showed that pyrimidine derivatives can be effective anti-COVID drugs [16]. Pyrimidine-based compounds are valuable due to their optical and physical properties. The organic π-conjugated molecular systems have semiconducting qualities and are used in optoelectronic devices [17], light emitting diodes (LED), field-effect transistors (FET) [18,19], sensors and solar cells [20] Organic field-effect transistors (OFETs) are used in electronic devices due to their cheapness, low weight, simple construction method, high flexibility, and environmentally friendly nature [21,22]. Pyrimidines were also applied as corrosion inhibitors [23], electroluminescent materials, and biomaterials in the past [24].

Phenylpyrimidine, which is part of the 4-Phenylpyrimidine (4-PPy), ($C_{10}H_8N_2$), molecule studied in this study, is a widely used basic skeleton due to its physicochemical and pharmaceutical properties [25]. The spectroscopic and electronic or optical properties of 4-Phenylpyrimidine, which describe its structure and have significant qualities, have not yet been studied in the literature.

The aim of the present work was to describe and characterize the molecular structure, spectroscopic properties, and some electronic structure properties of the title compound, both experimentally and theoretically. In this study, chemical reactivity, quantum chemical descriptors, and vibration analysis of 4-PPy were studied. Conformal analysis was performed to find the most stable conformer. A detailed vibrational analysis of the title compound was performed using the experimental FT-IR, FT-Raman, and Uv-Vis spectra, as well as the corresponding DFT data. ELF and LOL analyses were performed. The COVİD-19 pandemics caused by SARS-CoV-19 and the shortage of targeted drugs have forced scientists to look for new antiviral drugs. Heterocyclic compounds

E-mail address: sibelcelik@ahievran.edu.tr

https://doi.org/10.1016/j.molstruc.2022.134895
0022-2860/

containing nitrogen atoms have shown effective antiviral activities [26]. It has been stated in previous studies that pyrimidine derivatives can be effective anti-COVID drugs. Therefore, we showed that, using in silico molecular docking, the pyrimidine derivative structure can be inhibited by the core protease proteins of COVID-19. The graphical distribution of Frontier Molecular Orbitals (FMOs), along with other chemical and non-linear optical properties in both gaseous and liquid phases. Besides, the local reactivity was investigated using molecular electrostatic potential (MEP). The net electron transfer from donors to acceptors was evaluated using NBO analysis.

2. Material and methods

2.1. Computational methods

The Gaussian 09 W program package [27] was used for all the calculated theoretical properties of the title molecule. First, the optimized geometry of the molecule was obtained using the DFT/B3LYP theory approach with the 6-311++G(d,p) basis set. By solving the self-consistent field equation, the equilibrium geometry, corresponding to the true minimum on the potential energy surface (PES), was obtained effectively. The vibrational wavenumbers of the obtained lowest energy conformation were calculated at the same level of the theory. PQS (Parallel Quantum Solutions) software [28] was used to calculate the total energy distribution (TED). The calculated frequencies were scaled by 0.955 and 0.990 for wavenumbers below 1800 cm^{-1} and above 1800 cm^{-1}, respectively. HOMO, LUMO, and MEP analysis were visualized using GaussView 5.0 [29]. The Natural Bond Orbital (NBO) calculations were performed using the NBO 3.0 program [30]. The Multiwfn software program [31] is used to do the ELF and LOL analyses. The Autodock 2.2.6 software was used to molecular docking the chemical ligand-protein binding site [32]. The COVID-19 protein 3D structures were retrieved from the RCSB PDB database (http://www.rcsb.org). The 2D and 3D schematics, which were created by importing the docking results into the Discovery Studio Visualizer [33] and Chimera [34], illustrate the interactions between the inhibitor and surrounding residues of the SARS-CoV-2 main protease.

2.2. Instrumentation for recording spectra

On the Bruker Vertex 80 FT-IR spectrometer, the 4-PPy compound infrared spectra were acquired between 4000 and 550 cm^{-1}. The Raman spectra were recorded using a Bruker RFS 27: Standalone FT-Raman Spectrometer with an InGaAs laser source at 1064 nm in the region 4000–400 cm^{-1}. An Agilent HP 8453 spectrophotometer was used to record the UV–Vis spectrum in a quartz cell using EtOH, MetOH, DMSO, and H_2O as the solvent.

3. Results and discussion

3.1. Conformer and structure analysis

The stability of the molecules is found to play the most significant role in theoretical investigations of organic compounds involving geometric parameters [35]. Before determining the structural, spectroscopic, and electronic properties of a molecule using the DFT approach, it is necessary to define its conformer structure at the minimum energy level. The energy values corresponding to the torsion angles between C_3-C_4 atoms were calculated at the B3LYP/6-311++G(d, p) level theory in steps of 10° from 0° to 180°. The conformer structure with the lowest energy (−495.5102392770 Hatree = −13483.62642711 eV) was obtained at 130°. Fig. 1 shows the energy values associated with torsion angle analysis. Optimization calculations of the title molecule in the gas phase and in other solvents (water, DMSO, and methanol) were performed on the lowest energy conformer structure obtained at 130°. In this study, the bond length and bond angle values for the most stable structure were calculated in the gas phase. These values are given in Table 1 and the optimized structure of 4-PPy is presented in Fig. 2. For this study, we couldn't get the crystal structure of the molecule from the title, so we compared the bond lengths and angles to those in the crystal structure of 2-(4-nitrophenyl)−4-phenylpyrimidine [36].

The N_1-C_4, N_1-C_{12}, N_2-C_{11}, and N_2-C_{12} bond lengths in the pyrimidine ring of the title molecule are calculated as 1.345, 1.331, 1.337, and 1.335 Å, respectively. The C–C bond lengths in the phenyl and pyrimidine rings have values between 1.387 and 1.484 Å, while the C–H bond lengths have values between 1.082 and 1.087 Å. As can be seen from Table 1, the values of the

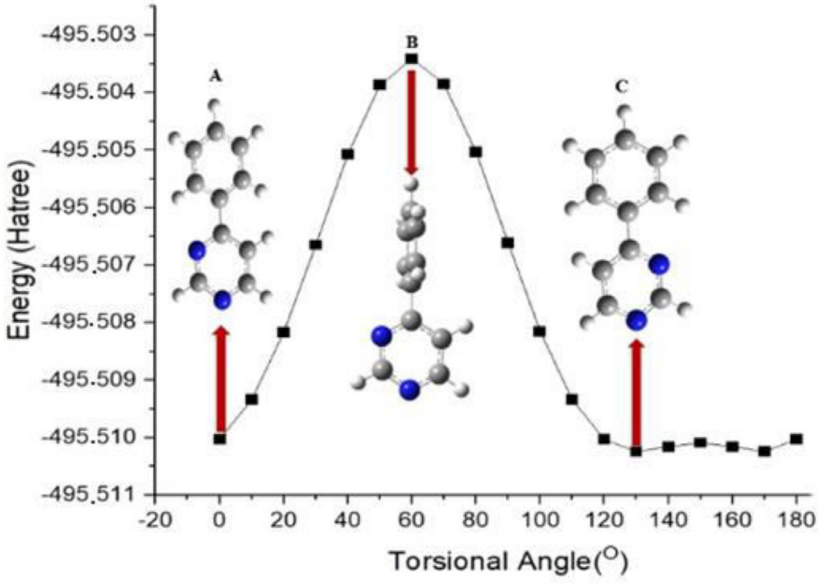

Fig. 1. Energy values corresponding to torsion angles in conformer structure analysis.

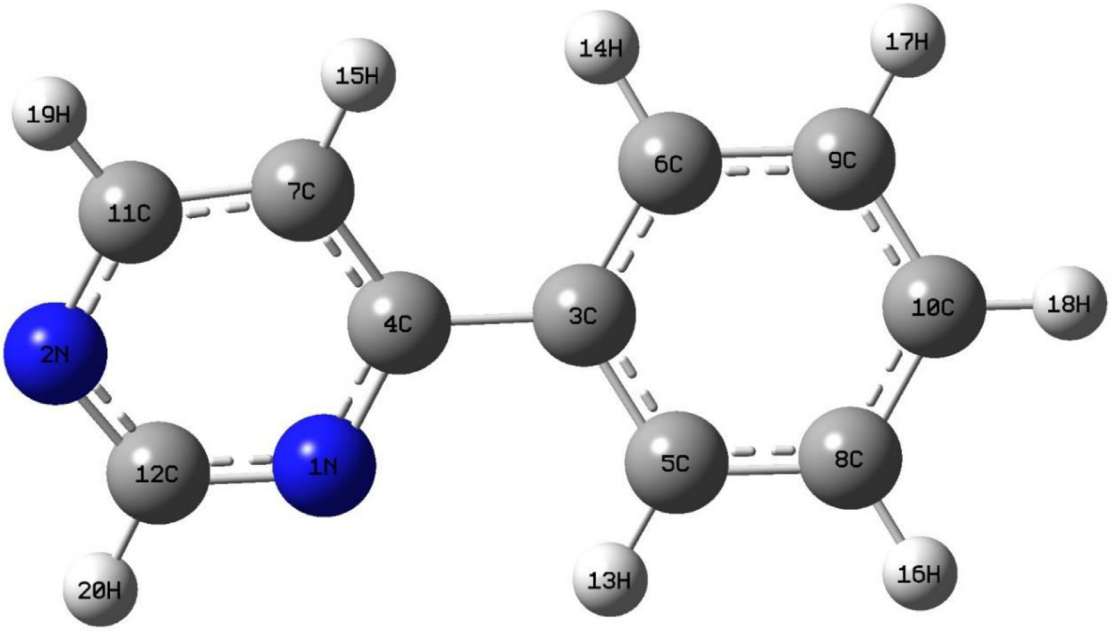

Fig. 2. Optimized geometric structure of 4-PPy by using B3LYP/6-311G++(d,p) level.

Table 1
Optimized geometrical parameters of 4-PPy obtained by B3LYP/6-311++G (d,p) basis set in the gas phase and in comparison with geometrical parameters of 2-(4-nitrophenyl)−4-phenylpyrimidine.

Parameters[a]	Bond Lengths (Å)		Parameters	Bond angles (°)	
	Calculation	XRD[b]		Calculation	XRD[b]
N_1-C_4	1.345	1.345	C_4-N_1-C_{12}	117.50	118.08
N_1-C_{12}	1.331	1.335	C_{11}-N_2-C_{12}	115.15	114.99
N_2-C_{11}	1.337	1.332	C_4-C_3-C_5	119.65	121.64
N_2-C_{12}	1.335	1.349	C_4-C_3-C_6	121.70	120.63
C_3-C_4	1.484	1.488	C_5-C_3-C_6	118.65	117.71
C_3-C_5	1.402	1.389	N_1-C_4-C_3	117.28	117.08
C_3-C_6	1.402	1.393	N_1-C_4-C_7	119.75	119.88
C_4-C_7	1.402	1.391	C_3-C_4-C_7	122.96	123.02
C_5-C_8	1.391	1.381	C_3-C_5-C_8	120.59	120.83
C_5-H_{13}	1.082	0.929	C_3-C_5-H_{13}	118.64	119.62
C_6-C_9	1.392	1.375	C_8-C_5-H_{13}	120.77	119.55
C_6-H_{14}	1.083	0.929	C_3-C_6-C_9	120.69	121.15
C_7-C_{11}	1.387	1.371	C_3-C_6-H_{14}	120.34	119.48
C_7-H_{15}	1.082	0.931	C_9-C_6-H_{14}	118.96	119.36
C_8-C_{10}	1.395	1.378	C_4-C_7-C_{11}	117.59	117.44
C_8-H_{16}	1.084	0.929	C_4-C_7-H_{15}	122.06	121.29
C_9-C_{10}	1.394	1.397	C_{11}-C_7-H_{15}	120.35	121.26
C_9-H_{17}	1.084	0.929	C_5-C_8-C_{10}	120.27	120.35
C_{10}-H_{18}	1.084	0.929	C_5-C_8-H_{16}	119.69	119.85
C_{11}-H_{19}	1.087	0.929	C_{10}-C_8-H_{16}	120.03	119.79
C_{12}-H_{20}	1.087	–	C_6-C_9-H_{17}	119.72	119.75
			C_{10}-C_9-H_{17}	119.72	119.78
			C_8-C_{10}-C_9	119.65	119.48
			C_8-C_{10}-H_{18}	120.22	120.18
			C_9-C_{10}-H_{18}	120.13	120.34
			N_2-C_{11}-C_7	122.77	123.83
			N_2-C_{11}-H_{19}	116.49	118.04
			C_7-C_{11}-H_{19}	120.75	118.12
			N_1-C_{12}-N_2	127.24	125.73
			N_1-C_{12}-H_{20}	116.32	–
			N_2-C_{12}-H_{20}	116.44	–

[a] The numbers appearing as subscripts in the abbreviations given as N_1-C_4 (1N-4C) are given in Fig. 2[b]. X-Ray values taken from Ref. [36].

bond lengths are quite compatible with the values in the crystal structure of 2-(4-nitrophenyl)−4-phenylpyrimidine. The C–C-C bond angle of 4-PPy is theoretically in the range of 118° to 121°, while the X-Ray range is in the range of 119° to 121° We observed a very slight deviation between the experimental and theoretical data. There are very small deviations between those of 2-(4-nitrophenyl)−4-phenylpyrimidine used for comparison with the bond angle values found for the optimized structure. The reasons for these low deviations for bond lengths and bond angles are that 2-(4-nitrophenyl) is attached to 4-PPy in the reference structure and that there is no interaction between atoms as in the crystal lattice.

In addition, because conformer C is in the global minimum energy state, it is more stable than other conformers. So, the conformer of the title compound with the least amount of energy was chosen to learn more about so that the theoretical vibrational analysis, electronic, chemical, and biological properties could be predicted.

3.2. Vibrational analysis

The 4-PPy molecule consists of 20 atoms and has 54 normal vibrational modes. Since Cs belongs to the point group, 36 of these normal modes are in-plane vibrations and 18 are out-of-plane vibrations. Experimental and calculated infrared and Raman spectra for the 4-PPy compound are recorded in the range between 400 and 4000 cm^{-1} and plotted with the calculated ones in Fig. 3 and 4. The observed and calculated wavenumbers as well as the probable assignments of fundamental vibrational modes and%TED (Total Energy Distribution) values are given in Table 2. To assist in the assignment of the vibration bands, the estimated infrared and Raman spectra obtained using the DFT approach are compared.

C–H vibrations: For mono-substituted phenyl and pyrimidine aromatic rings, the CH stretching modes are expected above 3000 cm^{-1}. The heteroaromatic structure indicates the presence of stretching vibrations in the region of 3100–3000 cm^{-1}, which is the characteristic region for the identification of C–H stretching vibrations [37]. The 4-PPy molecule contains eight hydrogen-bonded pyridine rings and thus has eight C–H stretching vibrations. The theoretical frequency values estimated by DFT calculation are 3048, 3056, 3060, 3069, 3079, 3087, 3101, and 3102 cm^{-1}, respectively. These vibrations were observed at 3026, 3058, and 3086 cm^{-1} in the FT-IR spectrum and at 3033, 3068 cm^{-1} in the FT-Raman spectrum [38].

Table 2
Calculated and Experimental IR and Raman frequencies and total energy distributions of the 4-PPy molecule.

	Calculated	Observed					
Mod	Freq	Freq*	I_{IR}***	I_{RA}***	FT-IR	FT-Raman	TED%**
υ_1	39	37	0.4	100.0			$40\Gamma_{CCCC} + 37\Gamma_{CCCN} + 6\Gamma_{CCCH} + 2\Gamma_{NCCH}$
υ_2	92	89	0.0	3.4			$34\,\Gamma_{CCCC} + 27\Gamma_{CCCH} + 11\Gamma_{CCCN} + 3\Gamma_{CNCH} + 3\Gamma_{CNCN}$
υ_3	154	149	0.4	4.8		159m	$26\Gamma_{CCCC} + 23\Gamma_{CCCH} + 8\Gamma_{CCCN} + 8\Gamma_{CCNC} + 3\Gamma_{CNCH} + 3\Gamma_{HCCH} + 3\Gamma_{CNCN} + 12\delta_{CCC} + 3\delta_{CCN}$
υ_4	234	226	0.6	1.6		228w	$28\Gamma_{CCCC} + 27\Gamma_{CCCH} + 11\Gamma_{CCNC} + 9\Gamma_{CCCN} + 5\Gamma_{CNCH} + 5\Gamma_{CNCN}$
υ_5	325	314	0.0	1.2		319w	$15\upsilon_{CC} + 24\delta_{CCC} + 12\delta_{CCH} + 7\delta_{CCN} + 5\delta_{CNC} + 6\Gamma_{CCCC} + 5\Gamma_{CCCH} + 4\Gamma_{CCNC} + 3\Gamma_{CCCN} + 3\Gamma_{NCCH}$
υ_6	374	362	1.1	0.6			$15\Gamma_{CCCC} + 12\Gamma_{CCCH} + 17\Gamma_{CCCN} + 12\Gamma_{CNCH} + 4\Gamma_{HCCH} + 13\Gamma_{CCNC} + 7\Gamma_{NCCH} + 13\Gamma_{CNCN}$
υ_7	410	397	0.3	0.4			$6\delta_{CCC} + 27\Gamma_{CCCC} + 26\Gamma_{CCCH} + 6\Gamma_{CCCN} + 6\Gamma_{CNCH} + 4\Gamma_{HCCH} + 8\Gamma_{CCNC} + 4\Gamma_{NCCH} + 3\Gamma_{CNCN}$
υ_8	411	398	0.3	0.6			$37\Gamma_{CCCC} + 32\Gamma_{CCCH} + 6\Gamma_{CCCN} + 5\Gamma_{HCCH} + 4\Gamma_{CCNC}$
υ_9	475	460	2.4	0.1	436m	480w	$7\delta_{CCC} + 27\Gamma_{CCCC} + 23\Gamma_{CCCH} + 9\Gamma_{CCCN} + 6\Gamma_{CNCH} + 4\Gamma_{HCCH} + 7\Gamma_{CCNC} + 3\Gamma_{NCCH} + 3\Gamma_{CNCN}$
υ_10	578	559	0.4	0.9			$26\Gamma_{CCCC} + 23\Gamma_{CCCH} + 8\Gamma_{CCCN} + 12\Gamma_{CNCH} + 10\Gamma_{CCNC} + 5\Gamma_{NCCH} + 7\Gamma_{CNCN}$
υ_11	631	610	1.1	2.7			$7\upsilon_{CC} + 35\delta_{CCC} + 35\delta_{CCH} + 5\delta_{CCN} + 5\delta_{NCN}$
υ_12	638	617	6.4	0.3	618m		$7\upsilon_{CC} + 30\delta_{CCC} + 31\delta_{CCH} + 11\delta_{CCN} + 9\delta_{CNC}$
υ_13	694	671	5.2	1.8	673s		$5\upsilon_{CC} + 54 + 18\delta_{CCC} + 17\delta_{CCH} + 7\delta_{CCN} + 9\delta_{NCH} + 7\delta_{CNC} + 5\delta_{NCN} + 10\Gamma_{CCCC} + 7\Gamma_{CCCH}$
υ_14	703	680	12.0	0.0	685s		$37\Gamma_{CCCC} + 48\Gamma_{CCCH} + 4\Gamma_{CCCN}$
υ_15	762	737	21.8	0.3	738vs		$21\Gamma_{CCCC} + 40\Gamma_{CCCH} + 8\Gamma_{CCCN} + 7\Gamma_{CNCH} + 6\Gamma_{HCCH} + 7\Gamma_{CCNC} + 6\Gamma_{CNCN}$
υ_16	779	753	2.3	1.9	762m	764w	$18\upsilon_{CC} + 4\upsilon_{CN} + 21\delta_{CCC} + 21\delta_{CCH} + 5\delta_{CCN} + 6\delta_{NCH} + 6\delta_{CNC} + 5\delta_{NCN}$
υ_17	812	785	1.4	0.4	794m		$14\Gamma_{CCCC} + 24\Gamma_{CCCH} + 13\Gamma_{CCCN} + 4\Gamma_{CNCH} + 9\Gamma_{HCCH} + 8\Gamma_{CCNC} + 13\Gamma_{NCCH} + 10\Gamma_{CNCN}$
υ_18	855	826	2.5	0.5			$9\Gamma_{CCCC} + 53\Gamma_{CCCH} + 5\Gamma_{CCCN} + 5\Gamma_{CNCH} + 10\Gamma_{HCCH} + 7\Gamma_{NCCH}$
υ_19	862	834	8.5	0.3	848s		$6\Gamma_{CCCC} + 50\Gamma_{CCCH} + 6\Gamma_{CCCN} + 6\Gamma_{CNCH} + 11\Gamma_{HCCH} + 11\Gamma_{NCCH}$
υ_20	945	914	0.3	0.0			$10\Gamma_{CCCC} + 52\Gamma_{CCCH} + 4\Gamma_{CCCN} + 23\Gamma_{HCCH}$
υ_21	982	949	0.0	0.2			$19\Gamma_{CCCH} + 5\Gamma_{CCCN} + 22\Gamma_{CNCH} + 19\Gamma_{HCCH} + 8\Gamma_{CCNC} + 11\Gamma_{NCCH} + 8\Gamma_{CNCN}$
υ_22	991	959	0.3	0.2			$10\Gamma_{CCCH} + 49\Gamma_{CCCH} + 30\Gamma_{HCCH}$
υ_23	1007	974	1.2	1.3			$13\Gamma_{CCCH} + 34\Gamma_{CCCH} + 33\Gamma_{HCCH}$
υ_24	1009	976	1.6	3.6			$7\upsilon_{CC} + 7\upsilon_{CN} + 5\delta_{CCC} + 4\delta_{CCN}10\Gamma_{CCCH} + 27\Gamma_{CCCH} + 25\Gamma_{HCCH}$
υ_25	1016	982	2.2	5.4	983m		$5\upsilon_{CC} + 9\delta_{CCC} + 6\delta_{CCH} + 15\Gamma_{CCCH} + 5\Gamma_{CCCN} + 22\Gamma_{CNCH} + 6\Gamma_{NCCH} + 4\Gamma_{CNCN}$
υ_26	1017	984	0.8	1.0		987w	$10\upsilon_{CC} + 17\delta_{CCC} + 14\delta_{CCH} + 9\Gamma_{CCCH} + 14\Gamma_{CNCH} + 10\Gamma_{HCCH} + 5\Gamma_{NCCH}$
υ_27	1044	1010	1.0	5.9		1001s	$23\upsilon_{CC} + 23\delta_{CCC} + 28\delta_{CCH} + 5\delta_{CCN} + 5\delta_{CNC}$
υ_28	1076	1040	1.2	0.2		1025w	$19\upsilon_{CC} + 16\delta_{CCC} + 33\delta_{CCH} + 6\delta_{CCN} + 5\delta_{CNC}$
υ_29	1098	1062	0.4	0.2			$18\upsilon_{CC} + 6\upsilon_{CN} + 9\delta_{CCC} + 48\delta_{CCH}$
υ_30	1112	1076	2.3	0.7	1084m		$16\upsilon_{CC} + 9\upsilon_{CN} + 9\delta_{CCC} + 40\delta_{CCH} + 5\Gamma_{CCCH}$
υ_31	1183	1144	0.1	1.5			$13\upsilon_{CN} + 71\delta_{CCH}$
υ_32	1195	1156	1.2	1.1		1158w	$13\upsilon_{CC} + 12\upsilon_{CN} + 7\delta_{CCC} + 38\delta_{CCH} + 13\delta_{NCH}$
υ_33	1206	1166	1.6	3.4	1164m		$14\upsilon_{CC} + 6\upsilon_{CN} + 5\delta_{CCC} + 58\delta_{CCH} + 4\Gamma_{CCCH}$
υ_34	1224	1184	1.9	2.5			$19\upsilon_{CC} + 32\upsilon_{CN} + 6\delta_{CCC} + 19\delta_{CCH} + 8\delta_{NCH}$
υ_35	1303	1260	8.3	19.5			$29\upsilon_{CC} + 6\upsilon_{CN} + 8\delta_{CCC} + 36\delta_{CCH} + 4\delta_{CCN}$
υ_36	1321	1277	1.2	24.2	1280w	1298vs	$25\upsilon_{CC} + 8\upsilon_{CN} + 12\delta_{CCC} + 28\delta_{CCH} + 6\delta_{CCN} + 9\delta_{NCH}$
υ_37	1351	1307	2.8	0.1			$27\upsilon_{CC} + 6\upsilon_{CN} + 8\delta_{CCC} + 32\delta_{CCH} + 13\delta_{NCH}$
υ_38	1355	1310	2.4	0.5	1316m		$20\upsilon_{CC} + 4\delta_{CCC} + 63\delta_{CCH}$
υ_39	1419	1372	17.3	3.9	1387vs		$10\upsilon_{CC} + 15\upsilon_{CN} + 24\delta_{CCH} + 5\delta_{CCN}$
υ_40	1472	1424	5.5	1.4			$14\upsilon_{CC} + 6\upsilon_{CN} + 9\delta_{CCC} + 49\delta_{CCH} + 8\delta_{NCH}$
υ_41	1494	1445	3.6	1.6	1440w		$13\upsilon_{CC} + 11\upsilon_{CN} + 7\delta_{CCC} + 37\delta_{CCH} + 19\delta_{NCH}$
υ_42	1527	1477	5.3	6.0	1462s		$19\upsilon_{CC} + 5\upsilon_{CN} + 8\delta_{CCC} + 53\delta_{CCH} + 5\delta_{NCH}$
υ_43	1581	1529	20.3	0.4	1538vs		$15\upsilon_{CC} + 15\upsilon_{CN} + 10\delta_{CCC} + 34\delta_{CCH} + 7\delta_{NCH}$
υ_44	1614	1561	100.0	28.0			$20\upsilon_{CC} + 16\upsilon_{CN} + 4\delta_{CCC} + 21\delta_{CCH} + 8\delta_{CCN} + 17\delta_{NCH}$
υ_45	1623	1569	6.8	7.6	1569s	1570m	$20\upsilon_{CC} + 5\upsilon_{CN} + 19\delta_{CCC} + 35\delta_{CCH}$
υ_46	1642	1588	0.0	25.7	1598vw	1597vs	$31\upsilon_{CC} + 17\delta_{CCC} + 42\delta_{CCH}$
υ_47	3152	3048	1.9	5.9	3026w	2989m	$79\upsilon_{CH}$
υ_48	3160	3056	8.0	2.1		3033vw	$77\upsilon_{CH}$
υ_49	3165	3060	0.1	0.9	3058w		$81\upsilon_{CH}$
υ_50	3174	3069	2.5	5.2		3068m	$74\upsilon_{CH} + 6\delta_{CCH}$
υ_51	3184	3079	6.4	1.7			$5\upsilon_{CC} + 81\upsilon_{CH} + 4\delta_{CCC} + 5\delta_{CCH}$
υ_52	3192	3087	2.7	3.5	3086vw		$85\upsilon_{CH}$
υ_53	3207	3101	2.8	0.6			$80\upsilon_{CH}$
υ_54	3208	3102	1.0	3.3			$80\upsilon_{CH}$

C–C vibrations: The vibration frequencies observed in FT-IR at 1598, 1569, 1538, 1462, 1440, 1387, 1316, 1280, and 1164 cm^{-1} have been theoretically calculated to include stretching C–C vibrations, as well as vibrations such as stretching C–N, C–H and C–C bending. The strong bands are at 1598–1440 cm^{-1} in the observed spectrum. In the region of 760 to 600 cm^{-1}, C = C in-plane deformation predominates. Shimanouchi et al. support out-of-plane deformation turns below 600 cm^{-1}, which has a larger frequency than out-of-plane vibrations. The characteristic out of plane ring C–C bending is observed in the range of 600–420 cm^{-1}. IR peaks very close to these values were also determined experimentally [39,40].

C–N vibrations: C–N vibrations are difficult to identify due to the overlapping of other vibrations. In the present study, C–N stretching vibrations were observed at 1440, 1387, 1164, and 1084 cm^{-1} in FT-IR and 1298, 1158 cm^{-1} in FT-Raman spectrum. These wavenumbers were theoretically calculated at 1445, 1372, 1166, 1076, 1277, and 1156 cm^{-1}. According to the literature, C–N stretching vibrations are found to be well within their characteristic region [41,42].

3.3. Solvent effect on molecular descriptors

The HOMO and LUMO molecular orbitals are the electron-donating and electron-accepting capacities of a molecule or a system [43–45]. The difference in energy between these molecular orbitals is one of the most important things that determines how a molecule reacts, how hard or soft it is, and how reactive it is. In

Table 3
Calculated global reactivity descriptors (eV) of 4-PPy in different phase.

Molecular descriptors	Gas	Water	DMSO	Ethanol	Methanol
HOMO	−6.9860	−7.0565	−7.0551	−7.0529	−7.0537
LUMO	−2.0210	−2.0719	−2.0708	−2.0686	−2.0694
Energy Gap	4.9649	4.9846	4.9843	4.9843	4.9843
Ionization Potential	6.9860	7.0565	7.0551	7.0529	7.0537
Electron Affinity	2.0210	2.0718	2.0708	2.0686	2.0694
Global Hardness	2.4825	2.4923	2.4921	2.4921	2.4921
Electronegativity	4.5034	4.5641	4.5629	4.5607	4.5615
Chemical Potential	−4.5034	−4.5641	−4.5629	−4.5607	−4.5615
Global Softness	0.4028	0.4012	0.4012	0.4012	0.4012
Global Electrophilicity	4.0848	4.1792	4.1771	4.1732	4.1747

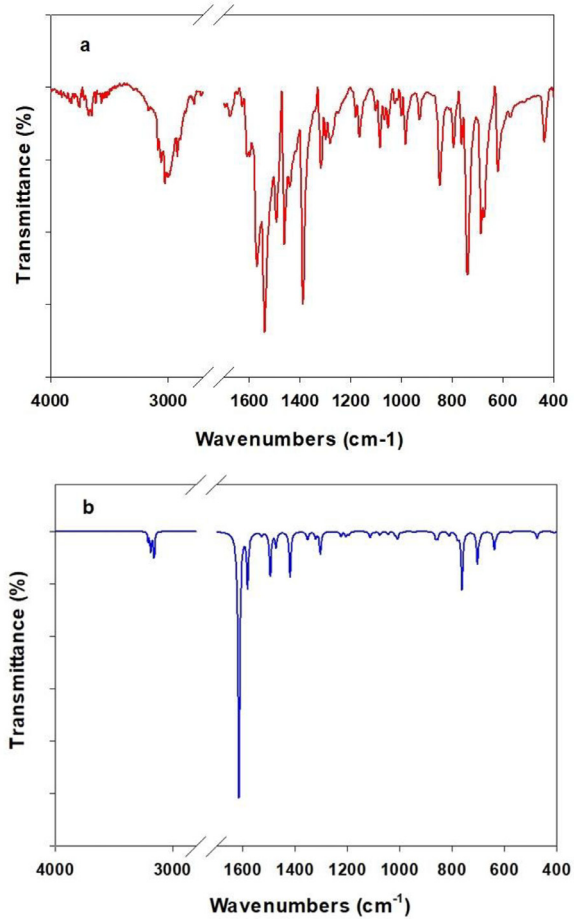

Fig. 3. Calculated IR and FT-IR graphs of the 4-PPy.

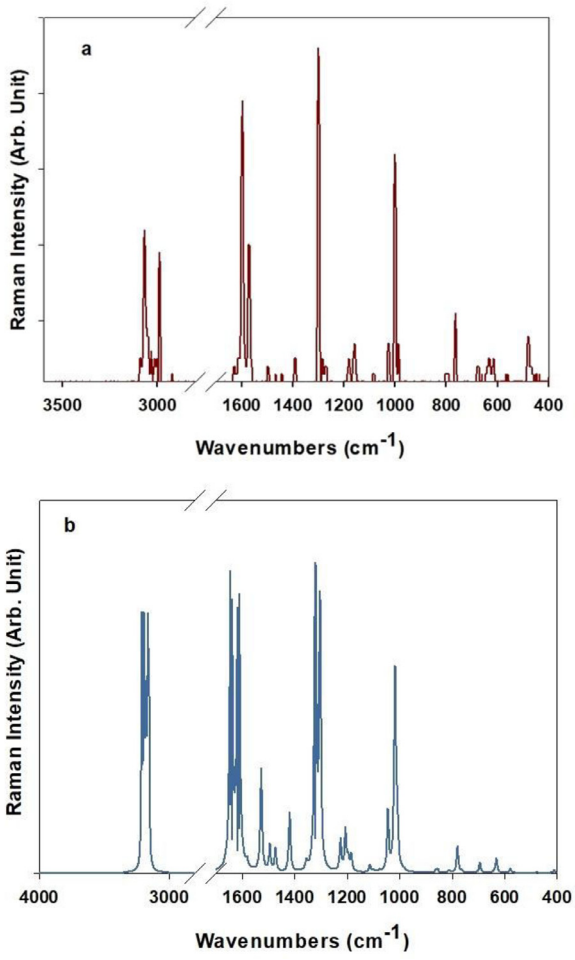

Fig. 4. Calculated Raman and FT-Raman graphs of the 4-PPy.

addition, the value of this energy gap is a property that also affects optical polarizability. Soft molecules need less energy to be excited, so they can be more easily polarized than hard molecules [46]. The HOMO and LUMO energies, as well as the other quantum chemical property values of 4-PPy, were calculated in the gas phase and in various solvents (water, DMSO, ethanol, and methanol) using B3LYP/6-311++ G(d,p) level theory. Energy values for the title molecule were presented in Table 3. The energies of the HOMO and LUMO molecular orbitals and the HOMO-LUMO energy gap in the gas phase were found to be −6.9860, −2.0210, and 4.9649 eV, respectively. In the calculations made in different solvents, due to the increase in the dielectric constant, the energy of the HOMO orbital decreased while the energy value of the LUMO orbital increased. As a result, the HOMO-LUMO energy gap values of the title compound in different solvents were found to be insignificantly larger than in the gas phase. The solvent-solute interaction becomes more stable in a solvent with a high dielectric constant because of hydrogen bonding and dipole-dipole interaction [47]. The energy gaps of the title molecule for water, DMSO, ethanol, and methanol solvents, respectively, were calculated as 4.9846, 4.9843, 4.9843, and 4.9843 eV. Chemical hardness values found in calculations made both in the gas phase and in different solvents show that this molecule has a hard structure and tends to have low chemical reactivity [48].

The HOMO and LUMO molecular orbital distributions of 4-PPy are given in Fig. 5. The HOMO and LUMO molecular orbital distributions were found to be the same as each other for the calculations made both in the gas phase and in the other solvents.

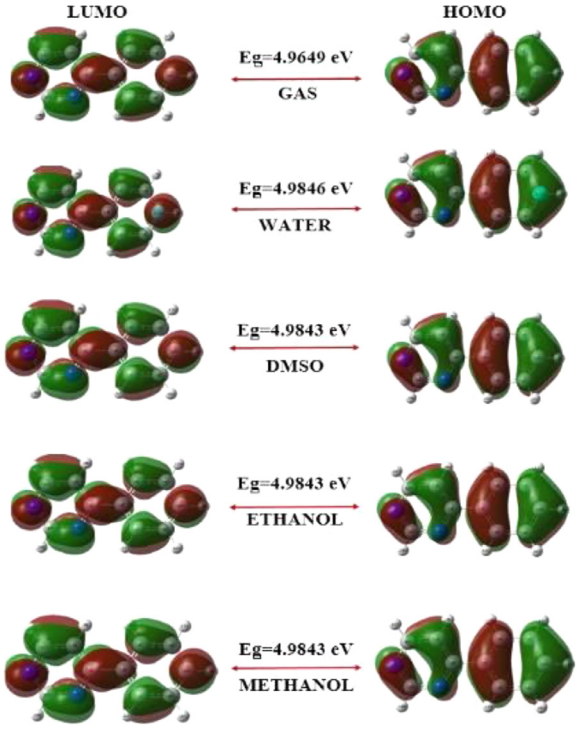

Fig. 5. 3D HOMO-LUMO molecular orbital distribution of 4-PPy in gas phase, water, DMSO, ethanol, and methanol solvents.

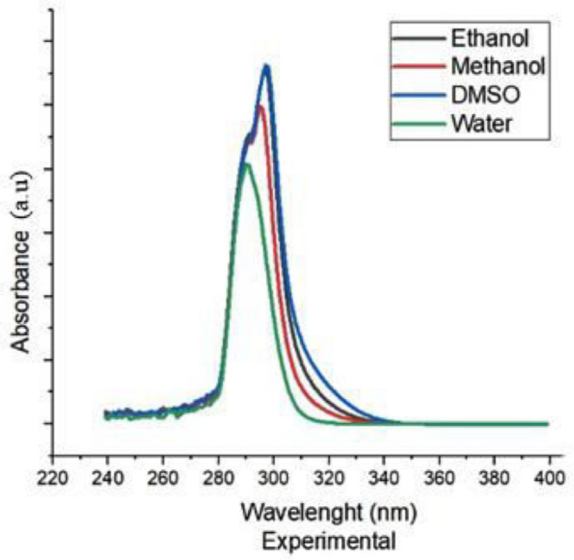

Fig. 6. UV–Vis spectra of 4-PPy compound.

3.4. UV–Vis spectrum of the compound

The ultraviolet spectra analysis of the title molecule 4PPy was investigated theoretically and experimentally. The UV–Vis spectrum was experimentally measured in four different solvents: EtOH, MeOH, DMSO, and H2O. On the basis of optimized ground-state geometric structures, TD-DFT/BLYP/B3LYP/6–311G(d,p) calculations have been used to determine the low-lying excited states of 4-PPy compound in different solvents. The experimental UV–Vis spectra of the molecule have been indicated in Fig. 6, and the peak values have been provided in Table 4. According to the computed results, the strongest signal in the electronic absorption spectrum

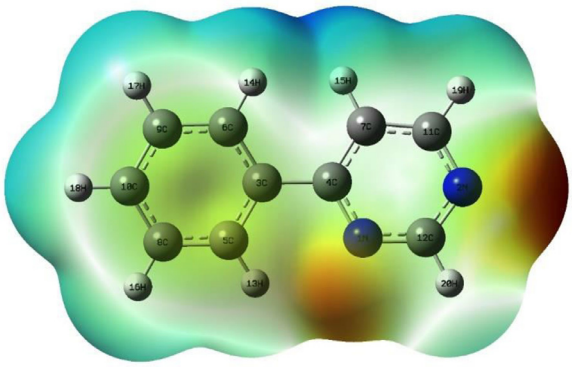

Fig. 7. Molecular electrostatic potential map of 4-PPy.

of molecule, 4-PPy, is calculated at a range 257-258 nm with oscillator strength $f = 0.587$, 0.58 and 0.601. The difference between the experimental and theoretical λ_{max} values in Table 4 may be due to the limitations of the TD-DFT calculations for load transfer systems. Another reason is that the effect of the geometry of the structure on the theoretical calculation cannot be ignored. While theoretical calculations were made using isolated geometry, experimental results were obtained for the bulk material. The experimental result includes interactions such as hydrogen bonding, van der Waals force, and electrostatic attraction in the lattice. Maximum oscillatory strength is observed at 257 nm and is assigned to HOMO→LUMO with symmetry = Singlet-A. Typically, according to the Frank-Condon principle, the maximum absorption peak (max) corresponds to vertical excitation in the UV–vis spectrum. Electron movement between these orbitals can occur easily. These excitations are associated with the π-π^* transition [49–51]. We can see that the transition with these double peaks is combined in the experimental results. Similar trend results were found for all solvent phases, which supports this situation in many studies [52,53].

3.5. Molecular electrostatic potantial (MEP) surface map analysis

A molecular electrostatic surface map helps to determine the electrophilic and nucleophilic regions of a molecule according to a color scale (order: red<orange< yellow< green < blue) [54,55]. In this color scale, electron-rich regions are represented in red, while electron-poor regions are shown in blue. Yellow and green colors represent less negative regions than red and neutral regions, respectively. For the gas phase, the molecular electrostatic potential map of 4-PPy is given in Fig. 7.

The N_2 and N_1 atoms in the pyrimidine ring of the title molecule are in the red region; that is, the most negative electrophilic region is localized on these atoms. The C atoms in the phenyl ring with the C_4 and C_{12} atoms in the pyrimidine ring of the title molecule are in the yellow (slightly electron-rich) region. H atoms are also located in the electron-poor blue region. According to the information obtained from the MEP map, we can say that the title molecule can enter a reaction, especially through N atoms.

3.6. Electron localization function and localized orbital locator analysis

The electron localization function (ELF) and the localized orbital locator (LOL) are maps that are used in surface analysis based on covalent bonds to determine regions with a high probability of finding electron pairs in molecular space [56]. ELF and LOL color maps for electron density charge distribution are presented

Table 4
Experimental and calculated UV–vis wavelength (λ), band gap energy (eV) and oscillator strength for the 4- PPy in solvents.

Solvent	Experimental	Theoretical				
	λ (nm)	λ (nm)	E (eV)	f	Symmetry	Major Contributions
Ethanol	310	257	4.81	0.587	Singlet-A	H L
		195	6.35	0.367	Singlet-A	H-1 *L* + 1H-1 *L* + 3
Methanol		257	4.55	0.579	Singlet-A	H L
		195	6.35	0.362	Singlet-A	H-1 *L* + 1H-1 *L* + 3
		257	4.81	0.58	Singlet-A	H L
Water		195	6.35	0.360	Singlet-A	H-1 *L* + 1H-1 *L* + 3
DMSO		258	4.80	0.601	Singlet-A	H L
		195	6.34	0.337	Singlet-A	H-1 *L* + 1H-1 *L* + 3

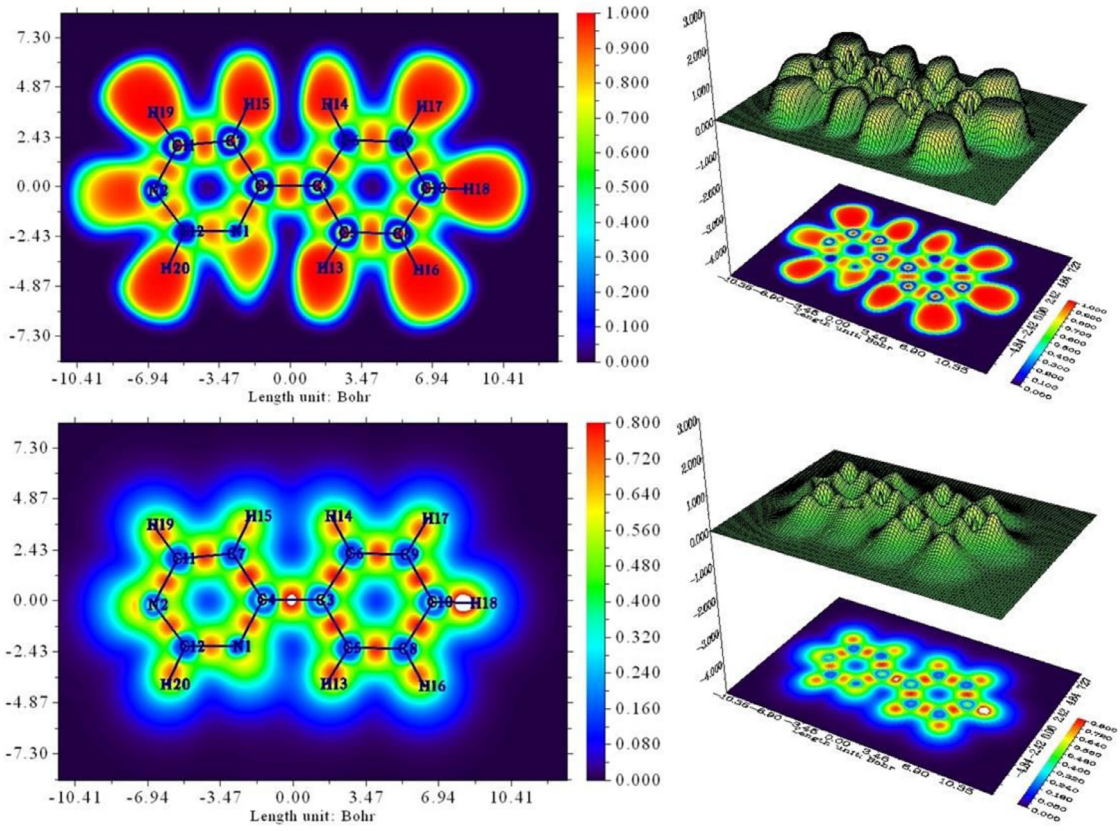

Fig. 8. Relif map and Color filled map of ELF and LOL of 4-PPy compound.

in Fig. 8. ELF has a value in the range of 0.00–1.0. The region between 0.5 and 1.0 represents the bound or unbound localized electrons, while the region below 0.5 defines the delocalized electrons. The red-colored regions indicate areas where the electrons are most highly localized. Therefore, we can say that electrons are localized in all hydrogen atoms. In addition, electrons are localized in the interatomic bond regions of the phenyl and pyrimidine rings. The blue regions around all the C and N atoms show the delocalized electron cloud. That is, this molecule will interact with other molecules or atoms from these regions. Similarly, in the localized orbital locator LOL map, electrons are localized between all H atoms and interatomic bond regions in the phenyl and pyrimidine rings, while delocalized electrons are found over all C and N atoms. According to molecular electrostatic potential surface map analysis, the most electrophilic regions are localized around the N_1 and N_2 atoms, while the slightly electron-rich regions are localized around all the C atoms in the phenyl ring and the C_4 and C_{12} atoms in the pyrimidine ring. The ELF, LOL, and MEP maps made to find the electrophilic and nucleophilic parts of the title molecule fit together very well.

3.7. Charge analysis

To support the data on electrophilic (negative) and nucleophilic (positive) regions obtained from MEP, ELF, and LOL maps of the title molecule, charge analyses were performed using the 6-311++ G(d,p) base set in the gas phase [57,58]. The atomic charge values obtained from atomic polar tensor (APT), Hirshfeld, and natural bond orbital (NBO) atomic charge analyses are presented in Fig. 9. In all three charge analyses, N atoms and all C atoms except C_4, C_{11}, and C_{12} atoms have negative values, while all H atoms also have positive values.

The results obtained from the atomic charge analysis are in high agreement with the MEP, ELF, and LOL maps. As a result, all of the analyses done to figure out where the negative and positive parts of the 4-PPy molecule were showed that the atoms with negative

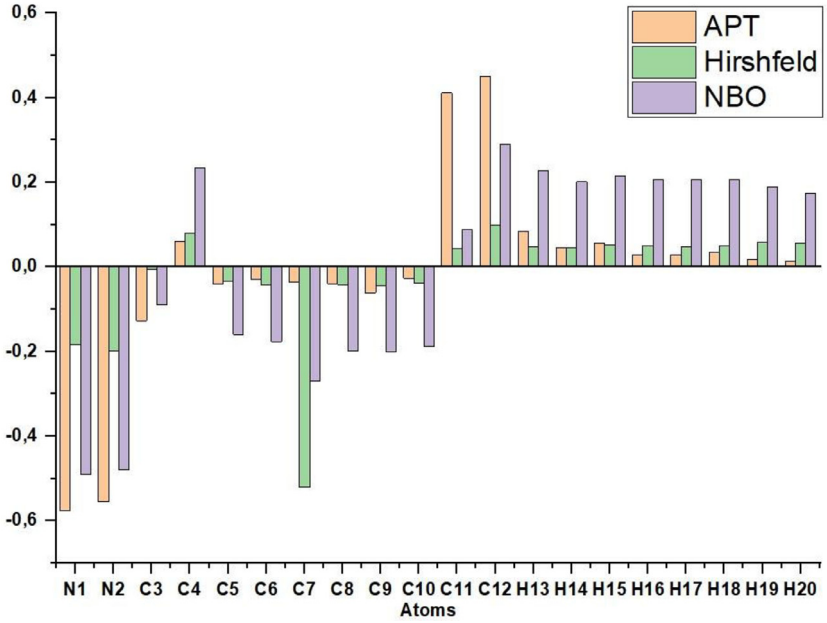

Fig. 9. APT, Hirshfeld, and NBO charges of the 4-PPy compound.

and positive values were almost the same, and the parts of the molecule where it could react were shown in detail.

3.8. Natural bond orbital (NBO) analyses

By calculating donor-acceptor pairings and donor-acceptor stabilization energy values with the NBO method, interactions in both occupied and virtual orbital fields are investigated in various chemical systems. The DFT/B3LYP/6-311++ G(d, p) method was used for the natural bond orbital analysis. $E^{(2)}$ energy is used to characterize the interaction between the receiver and the transmitter. It is calculated by the following equation:

In this equation, qi is the donor orbital population, εi and εj are the diagonal elements of the NBO orbitals. F (i, j) is defined as the off-diagonal NBO Fock matrix elements between the i and j NBO orbitals [59]. Table 5 presents the stabilization energies and interactions with an E(2) value above 5 kcal/mol.

When Table 5 is examined, $\pi*\rightarrow\pi*$ transitions for $N_1\text{-}C_4\rightarrow C_7\text{-}C_{11}$, $N_2\text{-}C_{12}\rightarrow C_7\text{-}C_{11}$, $N_1\text{-}C_4\rightarrow C_3\text{-}C_6$ have the strongest resonance energies with 216.94, 157.19, and 72.25 kcal/mol, respectively. These transitions occur as a result of intramolecular hyper-conjunctive interaction that causes significant delocalization in a system. Also, the results of NBO analysis, $\pi(N_1\text{-}C_4)\rightarrow\pi^*(N_2\text{-}C_{12})$, $\pi(C_7\text{-}C_{11})\rightarrow\pi^*(N_1\text{-}C_4)$, $\pi(N_2\text{-}C_{12})\rightarrow\pi^*(C_7\text{-}C_{11})$, $\pi(C_5\text{-}C_8)\rightarrow\pi^*(C_9\text{-}C_{10})$, $\pi(C_5\text{-}C_8)\rightarrow\pi^*(C_3\text{-}C_6)$, $\pi(C_9\text{-}C_{10})\rightarrow\pi^*(C_3\text{-}C_6)$, $\pi(C_9\text{-}C_{10})\rightarrow\pi^*(C_5\text{-}C_8)$, $\pi(C_3\text{-}C_6)\rightarrow\pi^*(C_9\text{-}C_{10})$, $\pi(C_3\text{-}C_6)\rightarrow\pi^*(C_5\text{-}C8)$, and $\pi(C_3\text{-}C_6)\rightarrow\pi^*(N_1\text{-}C_4)$ interactions gave strong stabilization energies for the title molecule. The interaction between lone pair and antibonding orbitals shows LP(1) $N_1\rightarrow\sigma^*(N_2\text{-}C_{12})$, LP(1) $N_1\rightarrow\sigma^*$ $(C_4\text{-}C_7)$, LP(1) $N2\rightarrow\sigma^*(N_1\text{-}C_{12})$, and LP(2) $N2\rightarrow\sigma^*(C_7\text{-}C_{11})$ interactions that give stabilization energies of 10.90, 9.48, 10.79, and 8.72 kcal/mol, respectively. Due to conjugative interactions, the transition σ(C12-H20)$\rightarrow\sigma^*(N_1\text{-}C_4)$ with a stabilization energy of 5.16 kcal/mol has also occurred for the title molecule.

3.9. Non-linear optical properties analysis

Recently, there has been increasing interest and significant competition in the field of optoelectronic, industrial, and optical data processing technologies for the technical applications of NLO materials. Therefore, it is very important to search for molecules with new NLO optical properties. The cheapest and most convenient method to predict the NLO properties of a molecule is to determine the dipole moment, polarizability, and hyperpolarizability values of the structure with the DFT calculation technique [60–62]. The solvent effect on the nonlinear optical properties of 4-PPy was investigated in this section of our study.

The dipole moment of a molecule or a system is induced and increased because the solvent effect has a curative effect on the delocalization of the charge in the molecules [47]. For this reason, it has also been reported in a previous study that the solvent energies of a molecular system are in correlation with its dielectric constants or dipole moments, and the dipole moment will be larger in solution than in the gas phase. As a result, the molecular system will be more stable [63]. Table 6 presents the dipole moment, polarizability, and initial hyperpolarizability values of 4-PPy in gas phase and polar solvents calculated in B3LYP/6-311++ G(d,p) using the IEFPCM model. The dipole moment increases in the solvation phase depending on the polarity of the solvent medium. The dipole moment value for 4-PPy in the gas phase was calculated as 2.777 Debye, while for water, DMSO, ethanol, and methanol it was calculated as 3.865, 3.840, 3.807 and 3.820 Debye. We found the HOMO-LUMO energy gap values for the gas phase and other solvents in the following order: Gas < DMSO= Ethanol= Methanol < Water. As a result, since the large charge in the molecule will be redistributed and there will be changes in the distances between the charge separations, the molecule has become more stable in the solvent, the HOMO-LUMO energy gap has increased, and the dipole moment values have increased [64].

Similarly, the first hyperpolarizability value of the title molecule also increased in different solvents compared to the gas phase. The first hyperplaizability value in the gas phase was found to be 5.908×10^{-30} esu. This value is approximately 15 times greater than the reference value of urea (0.3728×10^{-30}), which is used to determine the non-linear optical properties of a molecule. This value was found to be 17,333 × 10–^{30}, 17,106 × 10–^{30}, $16{,}642 \times 10^{-30}$, and $16{,}884 \times 10^{-30}$ esu for 4-PPy in water, DMSO, ethanol, and methanol solvents, respectively. These values are approximately 3 times higher than those of the gas phase and 45

Table 5 S
Table 5 Second Order Perturbation Theory Analysis of the most interacting NBO of 4-PPy.

Donor NBO (i)	Acceptor NBO (j)	E^2 (kcal/mol)[a]	ε_j-ε_i (a. u.)[b]	F(i,j) (a. u.)[c]
$\pi^*(N_1\text{-}C_4)$	$\pi^*(C_7\text{-}C_{11})$	216.94	0.01	0.082
	$\pi^*(C_3\text{-}C_6)$	72.25	0.03	0.066
$\pi^*(N_2\text{-}C_{12})$	$\pi^*(C_7\text{-}C_{11})$	157.19	0.01	0.077
$\pi(N_1\text{-}C_4)$	$\pi^*(N_2\text{-}C_{12})$	36.03	0.30	0.094
	$\pi^*(C_7\text{-}C_{11})$	10.86	0.32	0.53
	$\pi^*(C_3\text{-}C_6)$	8.66	0.34	0.049
$\pi(C_7\text{-}C_{11})$	$\pi^*(N_1\text{-}C_4)$	31.07	0.27	0.083
	$\pi^*(N_2\text{-}C_{12})$	14.14	0.27	0.055
$\pi(N_2\text{-}C_{12})$	$\pi^*(C_7\text{-}C_{11})$	29.29	0.32	0.087
	$\pi^*(N_1\text{-}C_4)$	10.41	0.31	0.052
$\pi(C_5\text{-}C_8)$	$\pi^*(C_9\text{-}C_{10})$	21.40	0.28	0.069
	$\pi^*(C_3\text{-}C_6)$	19.98	0.28	0.067
$\pi(C_9\text{-}C_{10})$	$\pi^*(C_3\text{-}C_6)$	21.22	0.28	0.070
	$\pi^*(C_5\text{-}C_8)$	18.54	0.29	0.066
$\pi(C_3\text{-}C_6)$	$\pi^*(C_9\text{-}C_{10})$	19.76	0.28	0.067
	$\pi^*(C_5\text{-}C_8)$	19.31	0.29	0.068
	$\pi^*(N_1\text{-}C_4)$	18.88	0.25	0.062
$Lp(1)N_1$	$\sigma^*(N_2\text{-}C_{12})$	10.90	0.88	0.89
	$\sigma^*(C_4\text{-}C_7)$	9.48	0.89	0.083
$Lp(1)N_2$	$\sigma^*(N_1\text{-}C_{12})$	10.79	0.89	0.089
	$\sigma^*(C_7\text{-}C_{11})$	8.72	0.92	0.081
$\sigma(C_{12}\text{-}H_{20})$	$\sigma^*(N_1\text{-}C_4)$	5.16	1.04	0.065

σ : sigma bonds, π : pi bonds, LP: lone pairs, RY* Rydberg.
[a] $E^{(2)}$ means energy of hyper conjugative interactions.
[b] Energy difference between donor and acceptor i and j NBO orbitals.
[c] $F_{(i,j)}$ is the Fock matrix element between i and j NBO orbitals.

Table 6
The electric dipole moment μ (Debye), average polarizability $\bar{\alpha}$, anisotropy of polarizability $\Delta\alpha$ (10−24esu), and frst hyperpolarizability β (10−30esu) of the title molecule in the gas phase and the different solvents.

Parameters	Gas	Water	DMSO	Ethanol	Methanol
μ_x	2.130	2.794	2.784	2.764	2.775
μ_y	0.354	2.624	2.68	2.573	2.591
μ_z	0.354	0.490	0.487	0.481	0.484
μ	2.777	3.865	3.840	3.807	3.820
α_{xx}	29.098	39.395	39.24	38.920	39.087
α_{yx}	−0.136	−0.215	−0.214	−0.11	−0.212
α_{yy}	19.267	27.460	27.32	27.007	27.164
α_{zx}	−0.00563	−0.021	−0.0204	−0.0193	−0.0198
α_{zy}	−0.00537	0.012	0.108	0.00875	0.00980
α_{zz}	10.310	14.130	14.04	13.847	13.943
$\bar{\alpha}$	19.558	26.995	26.867	26.591	26.731
$\Delta\alpha$	16.278	21.894	21.839	21.723	21.788
β_{xxx}	−6.817	−19.430	−19.180	−18.66	−18.930
β_{xxy}	−0.0811	−0.398	−0.390	−0.372	−0.381
β_{yxy}	0.431	1.210	1.196	1.159	1.178
β_{yyy}	0.1530	−0.274	−0.257	−0.224	−0.241
β_{xxz}	−0.016	−0.078	−0.0763	−0.0724	−0.0743
β_{yxz}	−0.0932	0.389	0.378	0.357	0.368
β_{yyz}	−0.0036	−0.106	−0.102	−0.0942	−0.0982
β_{zxz}	0.482	0.898	0.887	0.866	0.876
β_{zyz}	0.149	0.103	0.106	0.111	0.108
β_{zzz}	0.0724	−0.058	0.0599	0.0628	0.0614
β_x	−5.904	−17.322	−17.097	−16.635	−16.884
β_y	0.2209	−0.569	−0.541	−0.485	−0.514
β_z	0.0523	−0.2424	−0.118	−0.1038	−0.111
β_{tot}	5.908	17.333	17.106	16.642	16.884
	0.0314	−0.1454	−0.0710	−0.0623	−0.0666

times higher than those of urea. According to these results, the 4-PPy molecule shows good non-linear optical properties both in the gas phase and in other solvents. In addition, the solvent effect increased the non-linear optical properties of this molecule [65].

3.10. Molecular docking study

Molecular docking is a type of bioinformatics modeling that involves the interaction of two or more molecules to produce a stable adduct [66]. Molecular docking predicts the binding geometry of a putative ligand to a target protein [67,68]. This is the theoretical evidence used to develop a molecule's structure and reactivity relationship [69]. Also, this method is important to save the time required for new drug discovery. Currently, researchers throughout the world are working on medications to treat the COVID-19 pandemic [70]. 4-PPy are N-based heterocyclic compounds with a diverse set of properties, several of which have been linked to antiviral activity [71]. A ligand is a molecule that acts as the complementary partner in the docking process [68,72]. Hence, it is crucial to evaluate their effectiveness against SARS-n-CoV-2. The molecular docking study was examined to investigate its efficacy in ligand binding to the against known COVID-19 (M^{pro}) proteins. The COVID-19 M^{pro} is a desirable drug target for antiviral drug design toward COVID-19 treatment because the M^{pro} is essential for polyprotein processing and virus maturation [73–75]. We tried to dock the 4-PPy with the three important proteins isolated from the virus. The protein structure of the SARS-CoV-2 main protease was obtained from the protein data bank (PDB IDs: 6LU7, 6W63, 6M03). Fig. 10 shows the interaction of the title molecule with selected proteins. In Table 7, binding energies obtained from in silico analysis results were compared with previously reported remdesivir triphosphate [76], known as a positive inhibitor of SARS-CoV-2. Remdesivir has been reported in the United States to improve the clinical state of COVID-19 patients and has received emergency usage approval for the treatment of COVID-19 [77,78]. As can be seen from the results, the best binding energy is between 4-PPy-6LU7 and, which is close to the binding energy of Remdesivir.

In addition, this value is significantly lower than the binding values of the reference drug for the other two proteins. However, the computed binding energies suggest that the 4-PPy molecule can spontaneously interact within the SARS-CoV-2 main protease binding site.

The docked pose clearly shows that the drug molecules bind within the active site of the SARS-CoV-2 main protease macromolecular structure. The results demonstrate that the ligand was bound to the main protease of SARSCoV-2 via many hydrophobic bonds and hydrogen interactions. It has already been reported that ligand binding with the receptor can possibly form H-bonds with important residues of its main protease [66]. As seen in

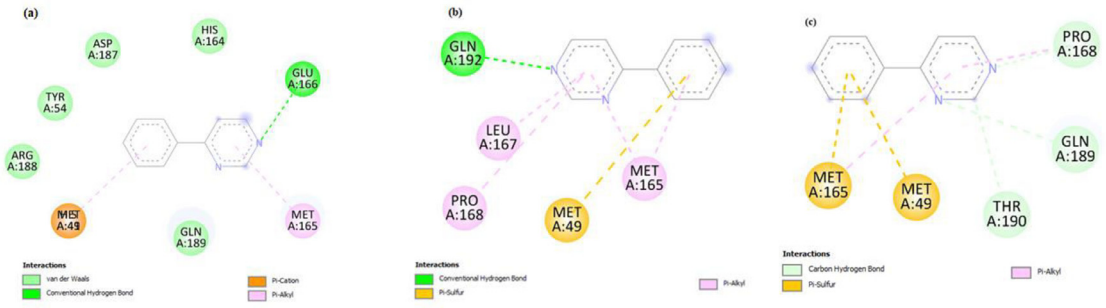

Fig. 10. 2D visualization of molecular interaction between 4-PPy and SARS- CoV-2 main protease (PDB ID: (a) 6LU7, (b) 6M03, (c) 6W63).

Table 7
Molecular docking result of 4-PPy compound with COVID-19 virus (M^{pro}) protease.

Compound	Protein(PDB ID)	Binding energy (kcal/mol)	Inhibition Constant K_i (μM)	Reference RMSD (Å)
4PPY	6LU7	−5.8	169.79	73.33
	6M03	−4.9	222.88	26.33
	6W63	−4.8	307.95	31.75
Remdesivir (Control)	6LU7	−6.5 [79]		
	6M03	−7.8 [76]		
	6W63	−7.6 [77]		

Tablo 8
The hydrogen bond interaction of title complex docked with the three protein targets.

Compound	Protein (PDB ID)	Hydrogen Bonded Amino Acid Residue	H-Bonded distance (Å)
[4-PPy]	6LU7	GLU A:166	2.22
	6M03	THR A:190GLN A:192	3.012.19
	6W63	THR A:190GLN A:189	2.672.82

Fig. 10, Fig. S1, and Table 8, an H-bond was formed with amino acid residues of the 4PPy ligands GLU'166, THR'190, GLN'189, and GLN'192, which interact with coronavirus proteins. These H-bonds are formed between the nitrogen of the pyrimidine ring and amino acid residues. In addition, interactions such as hydrophobic interactions with MET49A, MET165A, LEU167A, PRO168A, and LEU167A were also observed (see Table S1). Usually, the standard drug is surrounded by similar residues in its interaction with selected proteins, suggesting that this molecule may inhibit viral replication of SARS-CoV-2 [69, 79-81].

Our research indicates that the chemical in question can interact with certain n-CoV-19 proteins (6M03, 6W63, and 6LU7) and inhibit their growth. The results of molecular docking require more clinical investigation and could potentially aid in the management of COVID pneumonitis.

4. Conclusion

In the present paper, experimental and theoretical studies on the spectroscopic behavior of 4-PPy were examined. The UV–Vis spectra exhibit a significant peak at 311 nm in all phases, and the homo-lumo energy gap is in agreement with the experimental and theoretical phases. The MEP and ELF analyses revealed that the most electronegative region is located around the nitrogen atoms of the pyrimidine ring. Considering the calculated NLO property results, the hyperpolarizability of the title molecule is greater than that of the reference material urea, and it shows good nonlinear optical properties both in the gas and solvent phases. The nucleophilic and electrophilic regions, as well as the electron density, aided in predicting and identifying the active site of the molecule's reactivity. Using NBO analysis, the stability and intramolecular charge delocalization were investigated. Maximum energy $E^{(2)}$ was 157.19 kcal/mol, which corresponds to π^*(N2-C12)→ $\pi \rightarrow^*$(C7-C11). The charge transfer usually takes place between C–C and C–N bonds, indicating that the studied molecule can be a sufficient bioactive agent. Molecular docking studies show that 4-PPy docks with three important coronavirus proteins, with an interaction leading to inhibition of virus proteins. So, if more research is done, it might be possible to use it in new drugs that are developed to treat COVID-19.

Ethics approval and consent to participate

Not applicable.

Consent for publication

Not applicable.

Availability of data and materials

The article files will be available upon request

Competing interests

The authors declare that there is no confict of interests.

Funding

This research received no external funding.

Authors' information

Vocational School of Health Services, Ahi Evran University, Kırşehir 40200, Turkey.

Declaration of Competing Interest

The authors declare that they have no known competing financial interests or personal relationships that could have appeared to influence the work reported in this paper.

CRediT authorship contribution statement

Sibel Celik: Conceptualization, Data curation, Formal analysis, Methodology, Software, Writing – original draft, Visualization, Validation.

Data Availability

No data was used for the research described in the article.

Acknowledgements

Not applicable.

Supplementary materials

Supplementary material associated with this article can be found, in the online version, at doi:10.1016/j.molstruc.2022.134895.

References

[1] H. Vural, A novel copper (II) complex containing pyrimidine-4-carboxylic acid: synthesis, crystal structure, DFT studies, and molecular docking, J. Mol. Struct. 1265 (2009) 133390.
[2] Y.F. Sui, D. Li, J. Wang, R.R.Y. Bheemanaboina, M.F. Ansari, L.L. Gan, C.H. Zhou, Design and biological evaluation of a novel type of potential multi-targeting antimicrobial sulfanilamide hybrids in combination of pyrimidine and azoles, Bioorg. Med. Chem. Lett. 30 (2020) 126982.
[3] J. Zhang, J.F. Peng, T. Wang, P. Wang, Z.T. Zhang, Synthesis, crystal structure, characterization and antifungal activity of pyrazolo[1,5-a]pyrimidines derivatives, J. Mol. Struct. 1120 (2016) 228–233.
[4] R.B. Bakr, A.A. Ghoneim, A.A. Azouz, Selective cyclooxygenase inhibition and ulcerogenic liability of some newly prepared anti-inflammatory agents having thiazolo[4,5-d]pyrimidine scaffold, Bioorg, Chem 88 (2019) 102964.
[5] O. Alam, S.A. Khan, N. Siddiqui, W. Ahsan, S.P. Verma, S.J. Gilani, Antihypertensive activity of newer 1,4-dihydro-5-pyrimidine carboxamides: synthesis and pharmacological evaluation, Eur. J. Med. Chem. 45 (2010) 5113–5119.
[6] J.B. Shi, J. Gao, Y.P. Wang, Q.Z. Yao, Synthesis and antiviral activity of 4H-[1,2,5]oxadiazolo[3,4-d]pyrimidine-5,7-dione 1-oxide nucleosides, Chin. Chem. Lett. 20 (2009) 404–406.
[7] T. Gazivoda, S. Raic-Mali, V. Krištafor, D. Makuc, J. Plavec, S. Bratulic, S. Kraljevic-Paveli, K. Pavelic, L. Naesens, G. Andrei, R. Snoeck, J. Balzarini, M. Mintas, Synthesis, cytostatic and anti-HIV evaluations of the new unsaturated acyclic C-5 pyrimidine nucleoside analogues, Bioorg. Med. Chem. 16 (2008) 5624–5634.
[8] F. Panahi, R. Yousefi, M.H. Mehraban, A. Khalafi-Nezhad, Synthesis of new pyrimidine-fused derivatives as potent and selective antidiabetic α-glucosidase inhibitors, Carbohydr. Res. 380 (2013) 81–91.
[9] K. Avasthi, N. Garg, T. Chandra, D.S. Bhakuni, P.P. Gupta, R.C. Srimal, Synthesis of 4-amino/hydroxy-6-methylthio-12-(2,2-diethoxyethyl)-1H/2H-pyrazolo[3,4-d]pyrimidines and their antiallergic activity, Eur. J. Med. Chem. 28 (1993) 585–591.
[10] L.P. Duan, Q.F. Zhao, H.B. Zhang, Novel 2H-[1,2,4]thiadiazolo[2,3-a]pyrimidine derivatives bearing chiral S(−)-2-(4-chlorophenyl)-3-methylbutyric acid moiety: design, synthesis and herbicidal activity, Arab. J. Chem. 3 (2010) 225–228.
[11] Z. Kökbudak, M. Saracoglu, S. Akkoç, Z. Çimen, M.I. Yilmazer, F. Kandemirli, Synthesis, cytotoxic activity and quantum chemical calculations of new 7-thioxopyrazolo[1,5-f]pyrimidin-2-one derivatives, J. Mol. Struct. 1202 (2020) 127261.
[12] H.G. Aslan, S. Akkoç, Z. Kökbudak, Anticancer activities of various new metal complexes prepared from a Schiff base on A549 cell line, Inorg, Chem. Commun 111 (2020) 107645.
[13] A. Thiriveedhi, R.V. Nadh, N. Srinivasu, Y. Bobde, B. Ghosh, K.V.G.C. Sekhar, Design, synthesis and anti-tumour activity of new pyrimidine-pyrrole appended triazoles, Toxicol. In. Vitro. 60 (2019) 87–96.
[14] A.A.H. Khlood, A.K. Yacoob, Synthesis and characterization of some New 2- and 6- substituted of 5- Acetyl - 4- (P- phenyl) pyrimidine and substituted thieno [2,3-d] pyrimidine, Univ. Aden. J. Nat. Appl. Sci. 25 (2021) 273–281.
[15] V. Sharma, N. Chitranshi, A.K. Agarwal, Significance and biological importance of pyrimidine in the microbial World, Int. J. Med. Chem. 2014 (2014) 1–31.
[16] J.S. Rane, P. Pandey, A. Chatterjee, R. Khan, A. Kumar, A. Prakash, S. Ray, Targeting virus-host interaction by novel pyrimidine derivative: an in-silico approach towards discovery of potential drug against COVID-19, J. Biomol. Struct. Dyn. 39 (2021) 5768–5778.
[17] S. Muhammad, A.G. Al-Sehemi, Z. Su, H. Xu, A. Irfan, A.R. Chaudhry, First principles study for the key electronic, optical and nonlinear optical properties of novel donor-acceptor chalcones, J. Mol. Graphics. Modell. 72 (2017) 58–69.
[18] S. Jungsuttiwong, R. Tarsang, Y. Surakhot, J. Khunchalee, T. Sudyoadsuk, V. Promarak, S. Namuangruk, Light-emitting diodes by band structure engineering in van der Waals heterostructures, Org. Electron. 13 (2012) 1836–1843.
[19] K. Walzer, B. Maennig, M. Pfeiffer, K. Leo, Highly efficient organic devices based on electrically doped transport layers, Chem. Rev. 107 (2007) 1233–1271.
[20] S. Günes, H. Neugebauer, N.S. Sariciftci, Conjugated polymer-based organic solar cells, Chem. Rev. 107 (2007) 1324–1338.
[21] L.L. Chua, J. Zaumseil, J.F. Chang, E.C.W. Ou, P.K.H. Ho, H. Sirringhaus, R.H. Friend, General observation of n-type field-effect behaviour in organic semiconductors, Nature 434 (2005) 194–199.
[22] A. Irfan, Modeling of efficient charge transfer materials of 4,6-di(thiophen-2-yl)pyrimidine derivatives: quantum chemical investigations, Comput. Mater. Sci. 81 (2014) 488–492.
[23] G. Bereket, C. Ögretir, M. Yaman, E. Hür, Tautomeric studies on 2-mercapto pyrimidines and their significance in corrosion process, J. Mol. Struct. 625 (2003) 31–38.
[24] P. Wei, X.D. Bi, Z. Wu, Z. Xu, Synthesis of triphenylamine-cored dendritic two-photon absorbing chromophores, Org. Lett. 7 (2005) 3199–3202.
[25] Y. Le, Y. Zhang, Q. Wang, N. Rao, D. Li, L. Liu, G. Ouyang, L. Yan, Microwave-assisted synthesis of phenylpyrimidine derivatives via Suzuki-Miyaura reactions in water, Tetrahed. Lett. 68 (2021) 152903.
[26] M.R. Aouad, D.J.O. Khan, M.A. Said, N.S. Al-Kaff, N. Rezki, A.A. Ali, N. Bouqellah, M. Hagar, Novel 1,2,3-triazole derivatives as potential inhibitors against Covid-19 main protease: synthesis, characterization, molecular docking and DFT studies, ChemistrySelect 6 (2021) 3468–3486.
[27] M.J. Frisch, G.W. Trucks, H.B. Schlegel, G.E. Scuseria, M.A. Robb, J.R. Cheeseman, G. Scalmani, V. Barone, B. Mennucci, G.A. Petersson, H. Nakatsuji, M. Caricato, X. Li, H.P. Hratchian, A.F. Izmaylov, J. Bloino, G. Zheng, J.L. Sonnenberg, M. Hada, M. Ehara, K. Toyota, R. Fukuda, J. Hasegawa, M. Ishida, T. Nakajima, Y. Honda, O. Kitao, H. Nakai, T. Vreven, J.A. Montgomery Jr., J.E. Peralta, F. Ogliaro, M. Bearpark, J.J. Heyd, E. Brothers, K.N. Kudin, V.N. Staroverov, R. Kobayashi, J. Normand, K. Raghavachari, A. Rendell, J.C. Burant, S.S. Iyengar, J. Tomasi, M. Cossi, N. Rega, J.M. Millam, M. Klene, J.E. Knox, J.B. Cross, V. Bakken, C. Adamo, J. Jaramillo, R. Gomperts, R.E. Stratmann, O. Yazyev, A.J. Austin, R. Cammi, C. Pomelli, J.W. Ochterski, R.L. Martin, K. Morokuma, V.G. Zakrzewski, G.A. Voth, P. Salvador, J.J. Dannenberg, S. Dapprich, A.D. Daniels, O. Farkas, J.B. Foresman, J.V. Ortiz, J. Cioslowski, D.J. Fox, Gaussian, Inc, 2009 Wallingford CT.
[28] P. Pulay, J. Baker, K. Wolinski, Green Acres Road, 2013 Suite AFayettevile, AR72703, USA.
[29] R. Dennington, T. Keith, J. Millam, GaussView, Version 5, Semichem Inc., Shawnee Mission, KS, 2009.
[30] E.D. Glendening, A.E. Reed, J.E. Carpenter, F. Weinhold, NBO 3.0 Program Manual Theoretical Chemistry Institute, University of Wisconsin, Madison, WI, 1996.
[31] T. Lu, F. Chen, Multiwfn: a multifunctional wavefunction analyzer, J. Comput. Chem. 33 (2012) 580–592.
[32] G.M. Morris, D.S. Goodwill, R.S. Halliday, R. Huey, W. Hart, R.K. Belew, A.J. Olson, J. Comput. Chem. 19 (1998) 1639–1662.
[33] BioviaVisualization.https://www.3ds.com/productsservices/biovia/products/molecular-modeling-simulation/biovia-discovery-studio/visualization/. (accessed 01 March 2022).
[34] T.D. Goddard, C.C. Huang, T.E. Ferrin, Visualizing density maps with UCSF Chimera, J. Struct. Biol. 157 (1) (2007) 281–287.
[35] S. Sevvanthi, S. Muthu, M. Raja, S. Aayisha, S. Janani, PES, molecular structure, spectroscopic (FT-IR, FT-Raman), electronic (UV–Vis, HOMO-LUMO), quantum chemical and biological (docking) studies on a potent membrane permeable inhibitor: dibenzoxepine derivative, Heliyon 6 (2020) e04724.
[36] Q. Gao, M. Wu, K. Zhang, M.Liu N.Yang, J. Li, L. Fang, S. Bai, Y. Xu, CCDC 1995256: Experimental Crystal Structure Determination, 2020.
[37] C. Kucuk, S. Yurdakul, B. Erdem, Experimental and theoretical Fourier transform infrared and Raman spectroscopy, density functional theory, antibacterial activity and molecular docking studies on 1(4methoxyphenyl)1Himidazole, Chem. Pap. 76 (2022) 2833–2854.
[38] S. Breda, I.D. Reva, L. Lapinski, M.J. Nowak, R. Fausto, Infrared spectra of pyrazine, pyrimidine and pyridazine in solid argon, J. Mol. Struct. 786 (2–3) (2006) 193–206.
[39] T. Shimanouchi, Y. Kakiuti, I. Gamo, OutofPlane CH vibrations of benzene derivatives, J. Chem. Phys. 25 (1956) 1245.
[40] M. Preuss, F. Bechstedt, Vibrational spectra of ammonia, benzene, and benzene adsorbed on Si (001) by first principles calculations with periodic boundary conditions, Phys. Rev. B 73 (2006) 155413.
[41] G. Świderski, R. Świsłocka, R. Łyszczek, S. Wojtulewski, M. Samsonowicz, W. Lewandowski, Thermal, spectroscopic, X-ray and theoretical studies of metal complexes (sodium, manganese, copper, nickel, cobalt and zinc) with pyrimidine-5-carboxylic and pyrimidine-2-carboxylic acids, J. Ther. Anal. Calorim. 138 (4) (2019) 2813–2837.
[42] D. Durga devi, S. Manivarman, S. Subashchandrabose, Synthesis, molecular characterization of pyrimidine derivative: a combined experimental and theoretical investigation, Karbala Inter. J. Modern. Sci. 3 (1) (2017) 18–28.
[43] A. Mahmood, A. Irfan, J.L. Wang, Machine learning for organic photovoltaic polymers: a minireview, Chin. J. Polym. Sci. 40 (2022) 870–876.

[44] A. Mahmood, M.Ali M.Saqib, M.I. Abdullah, B. Khalid, Theoretical investigation for the designing of novel antioxidants, Can. J. Chem. 91 (2) (2013) 126–130.
[45] C. Kucuk, S. Yurdakul, B. Erdem, Spectroscopic characterization, DFT calculations, and microbiological activity of 5-iodoindole, J. Mol. Struct. 1252 (2022) 132125.
[46] S. Kumar, A. Radha, M. Kour, R. Kumar, A. Chouaih, S.K. Pandey, DFT studies of disubstituted diphenyldithiophosphates of nickel(II): structural and some spectral parameters, J. Mol. Struct. 1185 (2019) 212–218.
[47] S. Celik, E. Tanıs, Toxic potential of Poly-hexamethylene biguanide hydrochloride (PHMB): a DFT, AIM and NCI analysis study with solvent effects, Comput. Theo. Chem. 1212 (2022) 113709.
[48] S.D. Oladipo, G.F. Tolufashe, C. Mocktar, B. Omondi, Ag(I) symmetrical N,N′ -diarylformamidine dithiocarbamate PPh3 complexes: synthesis, structural characterization, quantum chemical calculations and in vitro biological studies, Inorg. Chim. Acta 520 (2021) 120316.
[49] L.F. Cavalieri, A. Bendich, The ultraviolet absorption spectra of pyrimidines and purines, J. Amer. Chem. Soc. 72 (1950) 2587–2594.
[50] L.F. Cavalieri, A. Bendich, J.F. Tinker, G.B. Brown, Ultraviolet absorption spectra of purines, pyrimidines and triazolopyrimidines, J. Amer. Chem. Soc. 70 (1948) 3875–3880.
[51] H. Kılıç, UV/vis spectrophotometric determination of slow equilibrated N (1)-H missing deprotonation constant of a pyrimidine and thiopyrimidine: the final situation of the four pKa values, Spect. Acta Part A 229 (2020) 117867.
[52] A. Irfan, A. Mahmood, Computational designing of low energy gap small molecule acceptors for organic solar cells, J. Mex. Chem. Soc. 61 (4) (2017).
[53] A. Mahmood, A. Irfan, J.-.L. Wang, Molecular level understanding of the chalcogen atom effect on chalcogen-based polymers through electrostatic potential, non-covalent interactions, excited state behaviour, and radial distribution function, Polym. Chem 13 (2022) 5993–6001.
[54] M.A. Mumita, T.K. Pala, M.A. Alam, A.A.M. Islama, S. Paulb, M.C. Sheikh, DFT studies on vibrational and electronic spectra, HOMO–LUMO, MEP, HOMA, NBO and molecular docking analysis of benzyl-3N-(2,4,5-trimethoxyphenylmethylene) hydrazinecarbodithioate, J. Mol. Struct. 1220 (2020) 128715.
[55] S. Guidara, H. Feki, Y. Abid, vibrational Structural, M.E.P. NLO, NBO analysis and DFT calculation of bis 2,5-dimethylanilinium sulfate, J. Mol. Struct. 1080 (2015) 176–187.
[56] C. Kucuk, S. Yurdakul, Çelik S, B. Erdem, Experimental and DFT studies of 2-methyl-quinoxaline and its silver (I) complex: non-covalent interaction analysis, antimicrobial activity and molecular docking study, Inorg. Chem. Commun. 145 (2022) 109935.
[57] Y. Büyükmurat, S. Akyüz, Theoretical and experimental IR spectra and assignments of 3-aminopyridine, J. Mol. Struct. 563 (2001) 545–550.
[58] S. Yurdakul, E. Temel, O. Buyukgungor, Crystal structure, spectroscopic characterization, thermal properties and theoretical investigations on [Ag(methyl 4-pyridylketone)2NO3], J. Mol. Struct 1191 (2019) 301–313.
[59] J.J. Kores, I.A. Danish, T. Sasitha, J.G. Stuart, E.J. Pushpam, J.W. Jebaraj, Spectral, NBO, NLO, NCI, aromaticity and charge transfer analyses of anthracene-9,10-dicarboxaldehyde by DFT, Heliyon 7 (11) (2021) e08377.
[60] M.O. Senge, M. Fazekas, E.G.A. Notaras, W.J. Blau, M. Zawadzka, O.B. Locos, E.M.N. Mhuircheartaigh, Nonlinear optical properties of porphyrins, Adv, Mater 19 (2007) 2737–2774.
[61] S. Eryılmaz, N. Akdemir, E. İnkaya, The examination of molecular structure properties of 4,4′-oxydiphthalonitrile compound: combined spectral and computational analysis approaches, Spectrosc. Lett. 52 (2016) 28–42.
[62] R. Thomas, Y.S. Mary, K.S. Resmi, B. Narayana, S.B.K. Sarojini, S. Armakovic, S.S. Armakovic, G. Vijayakumar, C. Van Alsenoy, B.J. Mohan, Synthesis and spectroscopic study of two new pyrazole derivatives with detailed computational evaluation of their reactivity and pharmaceutical potential, J. Mol. Struct. 1181 (2019) 599–612.
[63] M. Marzieh, S. Abolfazl, P. Khalil, O.A. Reza, H. Farhad, DFT study and NBO analysis of solvation/substituent effects of 3-phenyl-benzo[d]thiazole-2(3H)-imine derivatives, J. Serb. Chem. Soc. 85 (11) (2020) 1445–1462.
[64] S. Kotiloğlu, S. Çelik, E. Tanış, M. Kurban, Investigation of structural, vibrational properties and electronic structure of fluorene-9-bisphenol: a DFT, ChemistrySelect 3 (2018) 5934–5940.
[65] M. Vennila, R. Rathikha, S. Muthu, A. Jeelani, R. Niranjana Devi, A. Irfan, Theoretical spectroscopic electronic elucidation with different solvents (IEF-PCM model), biological assessment and molecular docking studies on Moroxydine-Antiviral drug agent, J. Mol. Liq. 355 (2022) 118946.
[66] M.A. Hosen, N.S. Munia, M. Al-Ghorbani, M. Baashen, F.A. Almalki, T.B. Hadda, F. Ali, S. Mahmud, M.A. Saleh, H. Laaroussi, S.M.A. Kawsar, Synthesis, antimicrobial, molecular docking and molecular dynamics studies of lauroyl thymidine analogs against SARS-CoV-2: POM study and identification of the pharmacophore sites, Bioorg. Chem. 125 (2022) 105850.
[67] A. Tan, Novel 1, 2, 3-triazole compounds: synthesis, In vitro xanthine oxidase inhibitory activity, and molecular docking studies, J. Mol. Struct. 1211 (2020) 128060.
[68] M.Maria Julie, T. Prabhu, E. Elamuruguporchelvi, F.B. Asif, S. Muthu, A. Irfan, J. Mol. Liq. 336 (2021) 116335.
[69] F.A. Alharthi, N. Al-Zaqri, A. Alsalme, A. Al-Taleb, T. Pooventhiran, R. Thomas, D.J. Rao, Excited-state electronic properties, structural studies, noncovalent interactions, and inhibition of the novel severe acute respiratory syndrome coronavirus 2 proteins in Ripretinib by first-principle simulations, J. Mol. Liq. 324 (2021) 115134.
[70] C.Yorur Goreci, Synthesis and comparative spectroscopic studies, HOMO–LUMO analysis and molecular docking studies of 3,3′-(1,4-phenylene)bis[2-(6-chloropyridin-3-yl)prop2-enenitrile] based on DFT, J. Mol. Struct. 1263 (2022) 133149.
[71] N.M. Mahani, F. Mostaghni, H. Shafiekhani, Cuspareine as alkaloid against COVID-19 designed with ionic liquids: DFT and docking molecular approaches, J. Photochem. Photobio B 231 (2022) 112447.
[72] G. Bharathy, Johanan Christian Prasana, S. Muthu, Ahmad Irfan, Fazilath Basha Asif, A. Saral, S. Aayisha, R. Niranjana devi, J. Mol. Liq. 340 (2021) 117271.
[73] S. Celik, A.D. Demirag, A.E. Ozel, S. Akyuz, Interactions mechanism of commonly used drugs for the treatment of Covid-19, Bull. Chem. Soc. Ethiop. 4 (3) (2020) 613–623.
[74] M. Gadewar, B. Lal, Molecular docking and screening of drugs for 6lu7 protease inhibitor as a potential target for Covid-19, Inter. J. Appl. Pharm. 14 (1) (2022) 100–105.
[75] S. Celik, S. Akyuz, A.E. Ozel, Vibrational spectroscopic characterization and structural investigations of Cepharanthine, a natural alkaloid, J. Mol. Struct. 1258 (2022) 132693.
[76] M.C. Vlasiou, K.S. Pafti, Screening possible drug molecules for Covid-19. The example of vanadium (III/IV/V) complex molecules with computational chemistry and molecular docking, Comp. Toxicol. 18 (2021) 100157.
[77] I.N. Fitriani, W. Utami, A.T. Zikri, P. Santoso, In Silico Approach of Potential Phytochemical Inhibitor from Moringa oleifera, Cocos nucifera, Allium cepa, Psidium guajava, and Eucalyptus globulus for the treatment of COVID-19 by Molecular Docking, 2020, doi:10.21203/rs.3.rs-42747/v1.
[78] T.D. Silva Arouche, A.F. Reis, A.Y. Martins, J.F.S. Costa, R.N. Carvalho Junior, A.M.JC Neto, Interactions between remdesivir, ribavirin, favipiravir, galidesivir, hydroxychloroquine and chloroquine with fragment molecular of the COVID-19 main protease with inhibitor N3 complex (PDB ID: 6LU7) using molecular docking, J. Nanosci. Nanotechnol. 20 (12) (2020) 7311–7323.
[79] R.K. Mohapatra, L. Perekhoda, M. Azam, M. Suleiman, A.K. Sarangi, A. Semenets, L. Pintilie, S.I. Al-Resayes, Computational investigations of three main drugs and their comparison with synthesized compounds as potent inhibitors of SARS-CoV-2 main protease (Mpro): DFT, QSAR, molecular docking, and in silico toxicity analysis, J. King Saud Uni. – Sci. 33 (2021) 101315.
[80] R. Ramajayam, K.-.P. Tan, H.-.G. Liu, P.-.H. Liang, Synthesis, docking studies, and evaluation of pyrimidines as inhibitors of SARS-CoV 3CL protease, Bioorg. Med. Chem. Lett. 20 (2010) 3569–3572.
[81] M. Vijayakumar, B. Kannappan, P. Renganathan, S. Al-Ghamdi, M. Alsaidan, T. Ramesh, In silico identification of potential inhibitors against main protease of SARS-CoV-2 6LU7 from Andrographis panniculata via molecular docking, binding energy calculations and molecular dynamics simulation studies, Saudi J. Biol. Sci. 29 (1) (2022) 18–29.